ORIGINAL ARTICLE

CMT Joining of AA6061-T6 and AA6082-T6 and Examining Mechanical Properties and Microstructural Characterization

Yashwant Koli[1] · N. Yuvaraj[1] · S. Aravindan[2] · Vipin[1]

Abstract Nowadays, CMT is used for joining dissimilar thickness of dissimilar metals for achieving higher mechanical strength by using properties of both the metals. Joining of dissimilar aluminium alloys with dissimilar thickness by using gas metal arc welding with cold metal transfer (GMAW-CMT) process, is the primary objective of this work. CMT butt joining of 6061-T6 (3.18 mm) and 6082-T6 (2 mm) aluminium alloys was carried out by using ER4043 (Al–5%Si) wire. Mechanical properties and microstructural characterization were carried out for the weld bead. Microstructural examination at different weld zones is studied using optical microscope and field emission scanning electron microscope (FESEM). Macrostructural images were captured to study the weld bead geometry in relation to heat input. Mechanical properties were examined by Vicker's microhardness and tensile test (with reinforcement, that is, the actual profile of the bead and without reinforcement, that is, the profile of bead are flattened to the surface of the plate). The residual stresses were measured using high-resolution X-ray diffraction (HR-XRD) method. Results showed significant changes in mechanical properties when heat input was in the range of 120–130 J/mm. Removal of reinforcement height improved almost 7–11% of tensile strength. Compressive residual stresses were experienced in the weldment. Comparatively cold metal transfer (CMT) showed better residual stress results than metal inert gas (MIG) welding at the same heat input.

✉ Yashwant Koli
  yashwantkoli5@gmail.com

  N. Yuvaraj
  yuvraj@dce.ac.in

  S. Aravindan
  aravindan@mech.iitd.ac.in

  Vipin
  vipin@dce.ac.in

1 Department of Mechanical Engineering, DTU, Delhi 110042, India

2 Department of Mechanical Engineering, IIT Delhi, New Delhi 110016, India

1 Introduction

Cold metal transfer (CMT) is a new technique established on the foundation of its parent welding process, i.e. metal inert gas (MIG). As the word suggests, 'cold' refers to fusion welding technique only, but it has a very low 'thermal heat input' (THI) with negligible distortion due to nonzero current at the time of short circuiting [1]. The main innovation in CMT is in its wire movement assimilation. The digital process-control imposes the power supply each time when the short circuit occurs and controls the movement of wire's retraction. The liquid metal droplet on the tip of the wire is detached with the assistance of the wire retraction motion at the time of short circuiting. As opposed to MIG welding, electromagnetic force does not have any influence on the short circuiting of liquid metal droplet transfer with a recorded decrement in the heat input and weld spatter [2]. Thin aluminium sheets are used worldwide in every sector of the industry, especially in automotive because it is lightweight, durable and recyclable. Car manufacturers are now adopting this trend of rapidly developing thin aluminium alloy sheets, and these manufactured products are already achieving a positive

response in the market [3, 4]. It has been shown that the results are evidently proving that there is a reduction in measured weight of automobiles, for instance cars, buses, etc. During transportation, energy consumption is decreased by way of decreasing its total weight of the vehicle, which inevitably improves the engine's effectiveness. There are many different grades of aluminium, which are weldable, but especially 6XXX-series alloy is used for body parts of the vehicle, exterior and interior body panels, structural and weldable components that helps in reducing the weight of the vehicle [5–8]. Arc welding of aluminium alloy thin sheets possess distinctive difficulties, which can be ascribed to an increased coefficient of thermal expansion and conductivity with reference to steel. It is essential to avoid certain issues such as burning and distortion by controlling the heat input of the welds [3, 9]. It is difficult to achieve coalescence of thin sheets of aluminium by conventional MIG welding process due to the impediments such as dearth of control, over penetration and excessive spatter during the welding process. It constrains its use in the field, and as a result, expensive welding techniques have been used which inevitably increase the fabrication cost. Lower heat inputs have made short-circuit metal transfer a desirable method for joining thin sheets of aluminium [10].

CMT mode of operation provides a solution for welding thin sheets since it mitigates problems such as over-penetration, spattering, high heat input and distortion that come across MIG welding. The different kinds of materials and even different thickness of materials can be welded to realize the tailor welded blanks (TWB). Various benefits of TWBs in the field of vehicle design and manufacturing are part integration, weight reduction and enhancing structural properties. This fabrication technique has further delivered a new platform for the deployment of multiple automotive material system (MAMS) [11–14]. TWBs made of aluminium alloys make the fabricated components even lighter without compromising the strength requirement and structural complexity [15]. Recently, aluminium alloy TWBs are used to manufacture body parts such as bonnets, front doors and inner body parts of high-performance cars.

Moulton and Weckman [16] used double-sided arc welding (DSAW) for TWB applications with thin sheets of aluminium alloys. Beneficial results are found to facilitate aluminium alloy TWBs manufacturing. Liu et al. [15] made 6082 aluminium alloy TWBs from friction stir welding (FSW) with various thickness combinations for automotive applications. Results showed that TWBs are successfully formed by hot forming and cold die quenching (HFQ®) process, which helps in transforming into vehicle panel components. Forming and the subsequent ageing process are used to restore the degraded hardness of TWBs only when the cooling is faster than the critical cooling rate

of an alloy. Sterjovski et al. [17] used pulsed-tandem GMAW and experiences higher deposition with lower distortion for naval shipbuilding application. It is explained that naval surface ships with considerably less hull distortion reduce hydrodynamic drag, speed and fuel efficiency. İrizalp et al. [1] investigated the welding parameters by CMT method and mechanical behaviour of 2-mm-thick AA1050 sheet. Results exhibited the highest tensile strength and microhardness due to minimum heat input. Liu et al. [18] worked on AA2024-T3 joints and further revealed stress corrosion cracking at the intergranular level when subjected to constant loading condition. In welded specimens, it is observed that on subjection to compressive residual stress, there is a considerable reduction in crack growth rate, whereas when subjected to tensile stress, there is an incredible increase in local stress concentration factor, which has often been found as a leading factor to inter-granular stress corrosion cracking (IGSCC) throughout its service life. Shu et al. [19] investigated residual stress in a narrow gap welded joint of aluminium alloy by CMT. Results revealed that the final allocation of residual stress was evaluated based on the distribution of stress along various lines. Homogeneity was discovered in the stress field with stress concentrated on the weld metal and its neighbouring zones. Petroyiannis et al. [20] experimented with AA2024 hydrogen embrittlement induced by corrosion. Removal of oxidized areas mechanically almost restored ultimate and yield stress to their original values but ductility is not restored. Hydrogen evolution always occurs in the active growth of localized positions and cracks of corrosion. There is an observation of crack propagation of hydrogen embrittlement (HE), which can be resulted by hydrogen absorption into the alloy of aluminium [21]. Hermans and Den Ouden [10] worked towards achieving stability while performing short-circuit GMAW while accompanying the process behaviour. It has been brought into conclusion that to pursue maximum stability, a standard deviation of frequency should be kept minimum for short circuiting. Moreira et al. [22] used solid-state welding, i.e. friction stir welding (FSW), to join 6061-T6 and 6082-T6 aluminium alloys. It was able to produce lower yield and ultimate stress, and intermediate properties were shown by the dissimilar joints. Failures occurred close to the weld edge line in the tensile tests where minimum hardness value was perceived. Elrefaey and Ross [23] examined the microstructure and mechanical properties of similar (6082/6082 and 5182/5182) and dissimilar aluminium (6082/5182) alloys welded by CMT. Results showed that ER5356 and ER4043, both filler wire are compatible with AA6082 giving high strength, high ductility and low hardness. The HAZ microstructure showed fine precipitates of second phases and coarsening of the Mg_2Al_3 precipitates in the aluminium matrix for

5182 sheets, whereas HAZ of 6082 showed no change compared to the BM. Ahmad and Bakar [24] used the CMT welding method to join AA6061. Effect of post-weld heat treatment (PWHT) on mechanical and microstructural properties was examined. Results showed that PWHT produces a fine and uniform distribution of precipitates at the weld joints. Also, there is an increase in tensile strength, hardness and elongation by 3.8%, 25.6% and 21.5%, respectively.

Majority of the researchers/scientist working on CMT have preferred argon gas over helium credited to its low thermal conductivity (16.94 mW/m K) which provides deeper finger-like penetration profile. It is denser than air (density 1.7818 g/dm^3) which results in lower flow rates. Lastly, it has low ionization potential (15.7EV) facilitating better arc starting/stability which improves the quality of the weld by lowering chances of spatter. Aluminium alloys, specifically 6082-T6 and 6061-T6, are high strength Al–Mg(0.636 & 0.840)–Si(1.06 & 0.665) alloys that contain manganese (0.745 & 0.0676) to increase ductility and toughness used in trucks, canoes, railroad cars, furniture, pipelines, etc.

The main objective of this research work is to examine the mechanical properties and microstructural characterization of the dissimilar aluminium alloy CMT welded joint at different weld zones. Heat input plays a vital role in the joint efficiency and fracture.

2 Experiments

2.1 Methods and Material

Aluminium alloys of grade AA6082-T6 and AA6061-T6 were chosen of thickness 2 mm and 3.18 mm, respectively, for joining with the help of CMT welding machine TPS400i developed by Fronius as shown in Fig. 1a and b

and were operated for performing the experiments. Table 1 displays the chemical compositions (wt%) of substrate materials and filler materials obtained by chemical spectroscopy as per ASTM standards. Mechanical properties of substrate material are presented in Table 2. The microstructure of substrate material at 100× and 1000× optical zoom is shown in Fig. 2a–d, with the help of Olympus GX41 compact inverted metallurgical microscope which clearly shows the grain boundaries/structure (elongated grains). FESEM images are displayed in Fig. 2e–f which validates the images of optical microscope showing equiaxed grains in AA6061-T6 and elongated grains in AA6082-T6 along the rolling direction. XRD plots for parent materials are presented in Fig. 3a and b, which constitutes its primary elements like aluminium and silicon at various intensity. Figure 3c shows the tensile strength graphs of the substrate materials.

Single side butt joint with a negligible gap between the sheets having the bevel angle of 90° and dimension of 100 mm × 60 mm was fabricated. Before welding, each sample was cleaned with acetone and wire brush made of steel to remove the oxide film and other unwanted impurities from the welded surface. After preparing the surface, the samples were fastened in the fixture, as shown in the schematic diagram in Fig. 4. The argon gas (Ar) with 99.99% purity was used as a shielding gas at 15 L/min of flow rate which turned on to provide the arc stability.

Direct current electrode positive (DCEP) has been implemented in this CMT machine where welding torch which consists of wire electrode is coupled with the positive terminal of CMT power source and the base metal (BM) is coupled with the negative terminal, and it is also recognized as direct current reverse polarity (DCRP). DCEP/DCRP has been implemented because the electrons flowing from the negative terminal (workpiece) to the positive terminal (electrode wire) in the arc column help in
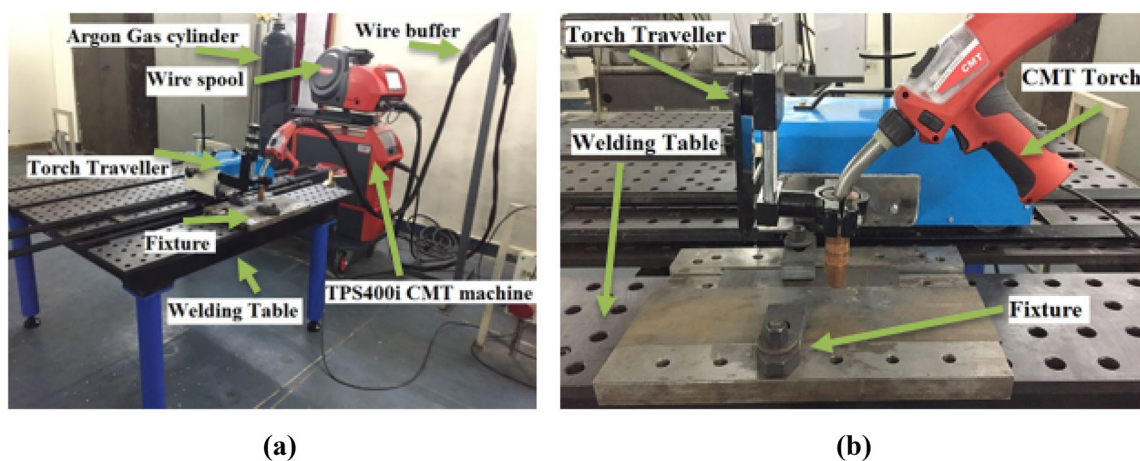

(a) **(b)**

Fig. 1 **a** and **b** TPS400i CMT machine

Table 1 Chemical compositions (wt%) obtained by chemical spectroscopy of substrate materials and filler wire as per ASTM standards

Elements	Al	Cu	Zn	Si	Mg	Fe	Mn	Cr	Ti
AA6082-T6	Bal.	< 0.0030	0.0045	1.06	0.636	0.189	0.745	0.0088	0.0184
AA6061-T6	Bal.	0.153	0.0226	0.665	0.840	0.253	0.0676	0.178	0.0225
ER4043	Bal.	0.3	0.10	5.6	0.05	0.8	0.05	0.05	0.02

Table 2 Mechanical properties of substrate material found experimentally

Properties	$\sigma_{0.2}$ (MPa)	σ_{UTS} (MPa)	δ (%)	$HV_{0.3N}$	Y (GPa)
AA6082-T6	269	304	20.1	109 ± 9	90 ± 7
AA6061-T6	247	284	24.9	116 ± 9	97 ± 4

$\sigma_{0.2}$ Tensile strength (TS) at 0.2% offset; σ_{UTS} Ultimate tensile strength (UTS); δ Elongation; $HV_{0.3N}$ Vicker's microhardness at 300 grams load; Y Young's modulus

Fig. 2 Optical images of substrate materials **a** AA6082-T6; **b** enlarged view of AA6082-T6; **c** AA6061-T6; **d** enlarged view of AA6061-T6; **e** and **f** FESEM images of AA6061-T6 and AA6082-T6, respectively
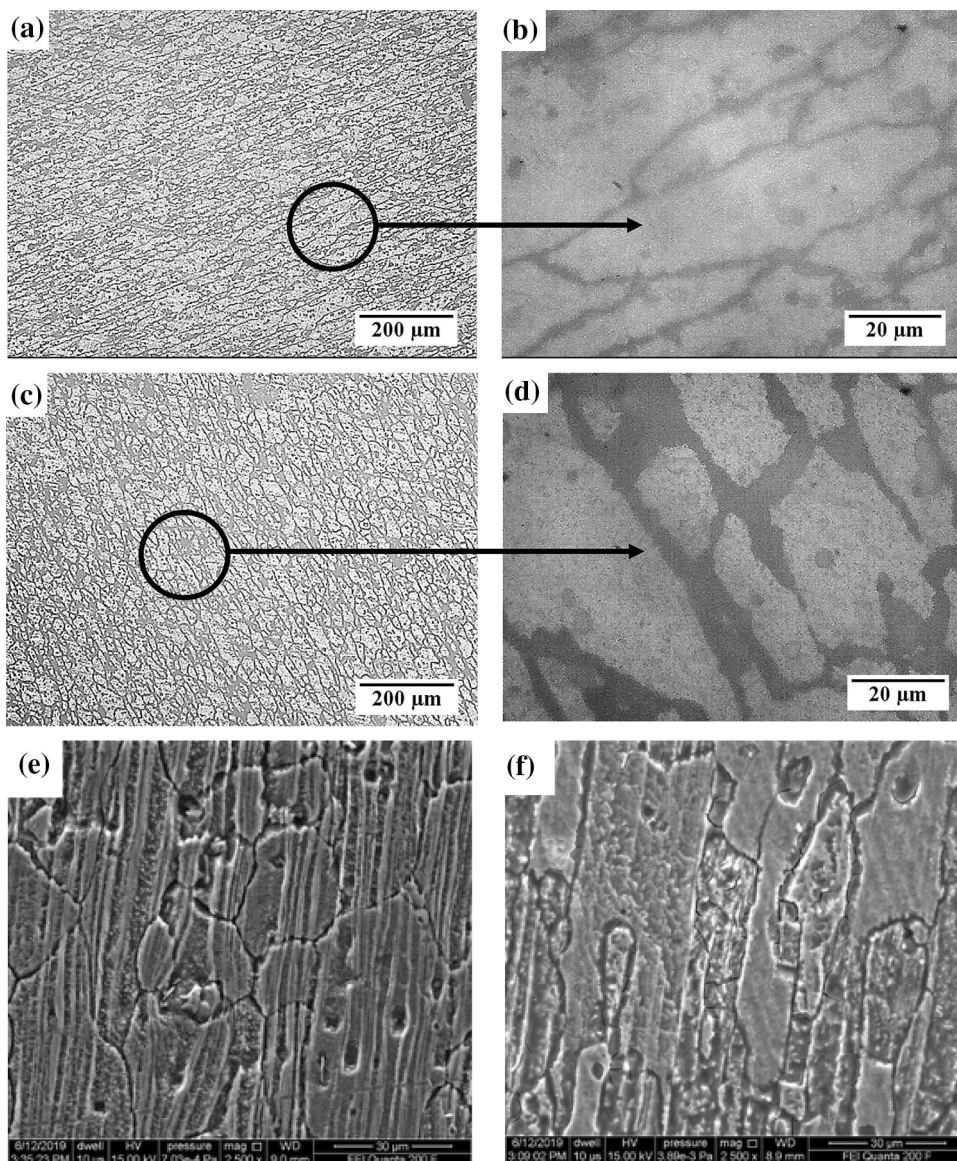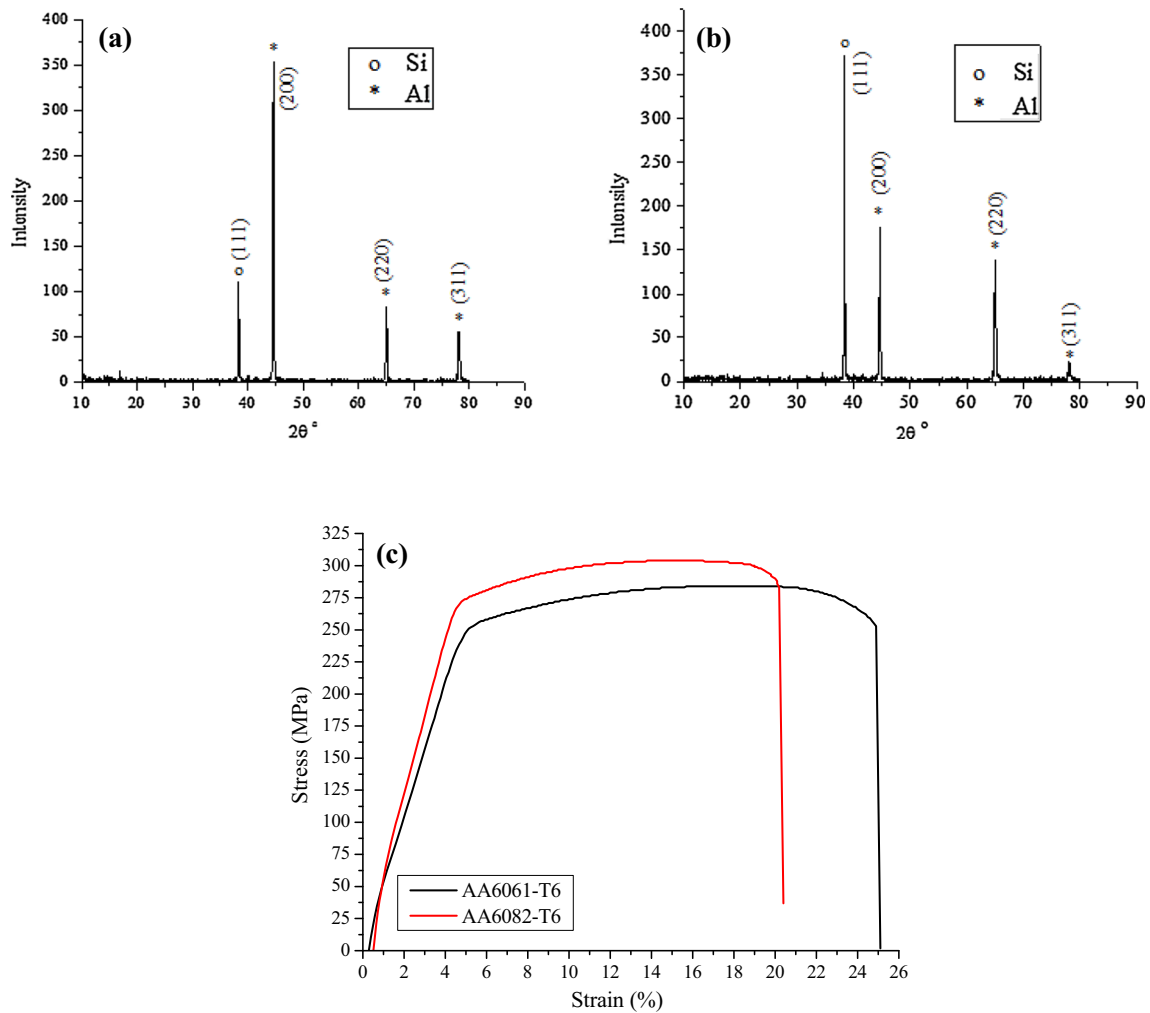
Fig. 3 XRD plots for the substrate materials a AA6061-T6; b AA6082-T6; c tensile strength graphs for substrate materials
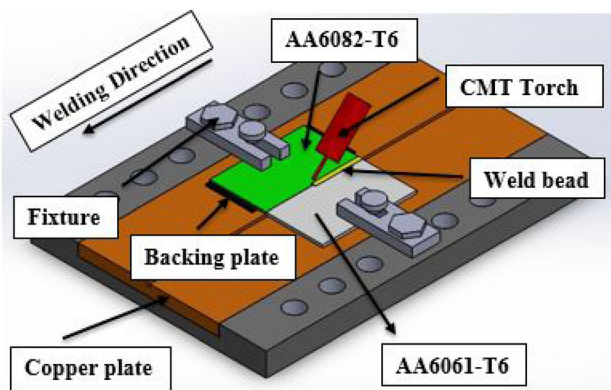

Fig. 4 Schematic diagram of the fixture

the uniform deposition. As the distance from the electrode to the base metal is much closer (i.e. CTWD), larger number of metal ions are mixed into the plasma arc column. These positive ions get attracted to the base metal, which strikes the same in a much hotter condition. This

results in more heat liberation in the BM compared with wire electrode tip helping to increase penetration. Direct current electrode negative (DCEN) results in thicker welds with an unstable arc and frequent arc outages. THI has a substantial influence on the weldment (WM) properties, and it has a huge consequence for the cooling rate of the WM [1]. It can be computed from the equation given below [25]. For a more economical method, the THI of the same joint needs to be reduced, resulting in stronger weld [26].

$$THI = \eta \cdot 60 \cdot \frac{VI}{S} \qquad (1)$$

where thermal heat input (J/mm), voltage (V), current (A) and welding/travel speed (mm/min) are represented by THI, V, I and S, respectively. Thermal efficiency (η) for MIG/CMT welding is taken as 80% standard [27, 28].

Table 3 Welding parameters of butt joint

| Sample	V (V)	I (A)	WFS (m/min)	S (mm/s)	H (J/mm)
1	11.2	61	4.2	5.5	99.37
2	11.3	66	4.7	5.5	108.48
3	11.5	72	5.1	5.5	120.43
4	12.2	78	5.4	5.5	138.41
5	12.2	78	5.4	6	126.88

Shielding gas is taken as 15 l/min. CTWD is taken as 10 mm. Arc length correction is taken as 0%

2.2 CMT Welding Mechanism

CMT offers the meticulous technique of material deposition and minimal THI by integrating a pioneering wire feed system (WFS) combined with high-speed digital control [9]. In the CMT process, the electrode wire is moved in the direction of the weld pool during an arcing period. When the wire tip of the electrode makes interaction with the molten weld pool, the arc column extinguishes, while the current dips to nonzero (i.e. tending to zero) which helps in avoiding any spatter generation. The consequence of dropping of the current is such that it significantly reduces the THI that is given by this process for the short-arc variation. With the help of this, it is feasible to weld thinner materials with a minimum amount of distortion, minimal rate of dilution and residual stresses in the WM [29–33]. The movement of wire is reversed by digital process control with the help of synergic power source, which aids droplet detachment during the 'short-circuiting phase' (SCP) [34]. The wire movement is withdrawn and the procedure commences again [35]. CMT process decreases the heat-affected zone (HAZ) owing to its minimal THI. Table 3 displays the input welding process parameters of each sample where 'S' denotes the welding/travelling speed and 'WFS' is the wire feed speed. In CMT welding of synergic lines, voltage (V), current (I) and wire feed speed (WFS) are inter-related to each other, i.e. by changing one of the above parameters, the rest two also change. For this experiment, the flow rate of shielding gas, CTWD and arc length correction (ALC) factor are taken as a constant value like 15 l/min, 10 mm and 0%, respectively. ALC is the factor, which corrects the arc length (i.e. allows even more precise control of heat input). It ranges from "− 10 to + 10%". The negative range is applied when shorter arc length is needed, that gives narrow weld bead with higher penetration by reducing the voltage. The positive range is applied when longer arc length is needed that gives wider weld bead with lower penetration by increasing the voltage. Zero is for neutral arc length (i.e. without any change in the correction factor).

With the help of Eq. 1, heat input is computed which is validated by the machine data which is created after every weld comprising of all the parameters. Bead profiles (top and bottom view) and cross-sectional macrostructure of respective samples are revealed in Fig. 5, with the help of vision inspection machine. The bead profiles (cross-section) were captured at $10\times$ magnification (8 mm), and this helps in determining the weld width, depth of penetration and height of reinforcement with respect to heat input as illustrated in Fig. 6. As shown in Fig. 5b, the penetration is not noticeable in sample 1 (61A and 5.5 mm/s) on the bottom side, but as the amount of current increases with increase in THI, the depth of penetration is evident in the latter samples in the bottom part of the plate. This amount of reinforcement with deeper finger-like penetration is achieved due to pure argon gas with a spatter less welding, which is a novelty of CMT. More and more volume of parent materials melt as current increases, keeping welding speed as a constant. It then fuses with the reinforcement material (ER4043) which increases the depth of penetration that results in an increment of dilution percentage. Visual inspection of the weld surface shows the negligible amount of spatter (Fig. 5), which validates the competence of CMT process to manufacture joints with essentially negligible amount of weld spatter. Cross-sectional macrostructure image is free from surface welding flaws such as cracks, lack of fusion, overlap and undercuts. It clearly shows the weld profile, fusion line, base metal side of AA6061-T6 and small amount of porosity seen in sample 3 (72A and 5.5 mm/s). Weld dimensions such as weld width (WW), penetration (WP) and reinforcement (WR) are calculated for all welded samples to demonstrate the different welding process parameters with the help of vision inspection machine as exemplified in Fig. 6. It is seen that weld width, penetration and reinforcement are in the range of 6.5–11 mm, 1.7–3.7 mm and 2.5–4.5 mm, respectively, w.r.t heat input. Weld width and penetration show an increasing trend (i.e. linear) with heat input. As heat input increases, more amount of substrate material comes in contact with arc, resulting in a wider width and deeper penetration. Weld reinforcement behaves as a decreasing

Fig. 5 Weld bead plate images (top and bottom) and cross-sectional view of macrostructures of respective sample **a–c** sample 1 (61A, 5.5 mm/s, 99.37 J/mm), **d–f** sample 2 (66A, 5.5 mm/s, 108.48 J/mm), **g–i** sample 3 (72A, 5.5 mm/s, 120.43 J/mm), **j–l** sample 4 (78A, 5.5 mm/s, 138.41 J/mm), **m–o** sample 5 (78A, 6 mm/s, 126.88 J/mm)
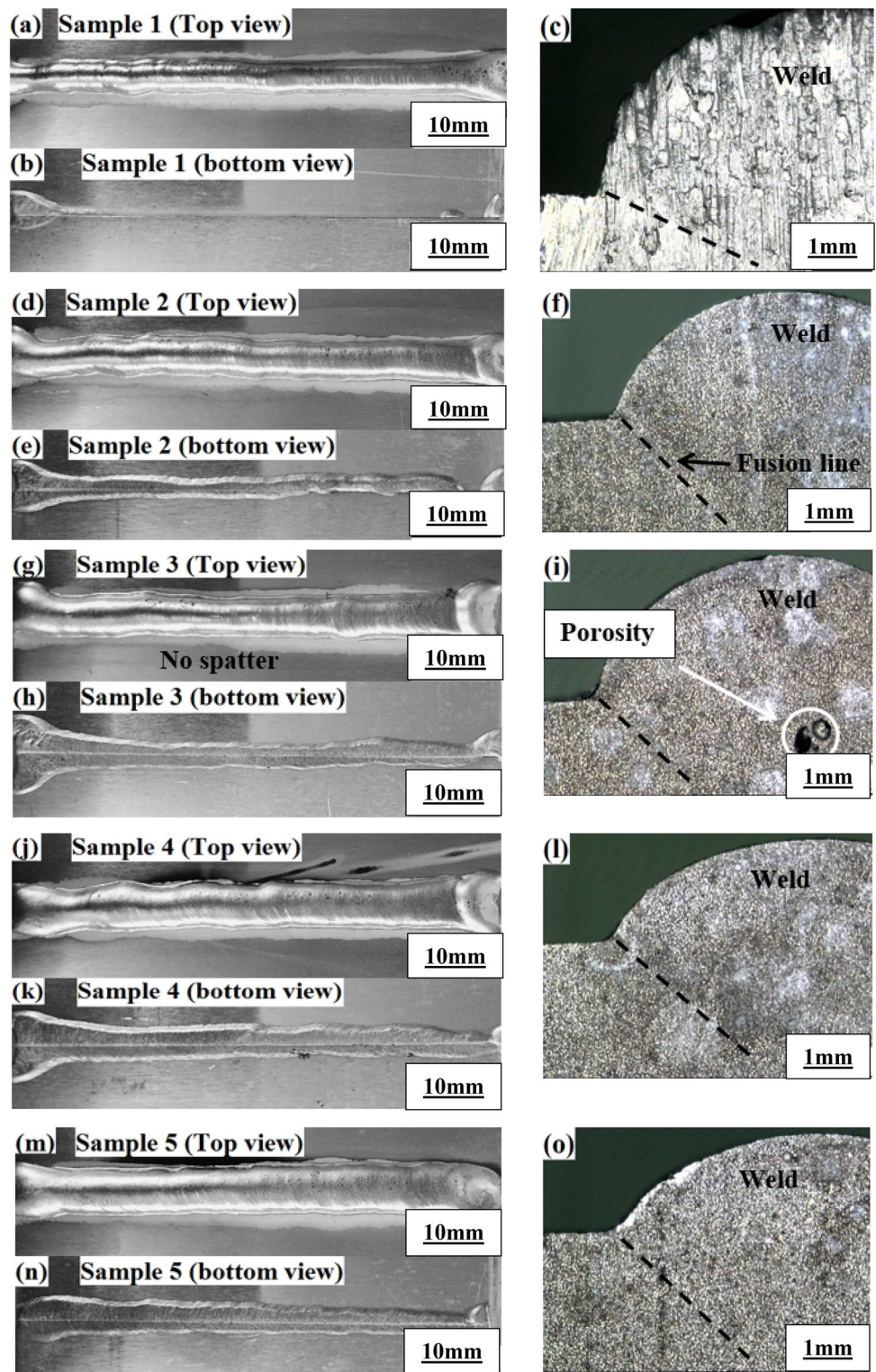
trend with maximum and minimum values being 4.3 mm and 2.7 mm, respectively. As heat input increases, weld reinforcement increases till 108 J/mm, and then, it rapidly decreases approaching a minimum value in the end. Higher the value of current, deeper will be the penetration with a wider width owing to relatively higher heat input. Heat input of 126.88 J/mm (78A, 6 mm/s) and 138.41 J/mm (78A, 5.5 mm/s) have a similar amount of current but different welding speed.
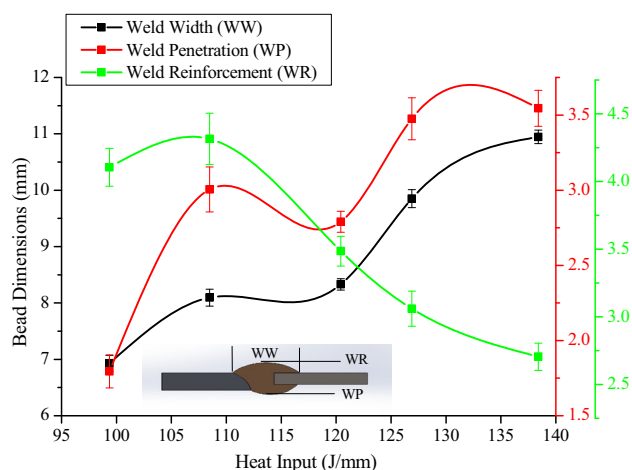
Fig. 6 Weld bead dimensions

EDX spectroscopy of sample 3 (72A, 5.5 mm/s) clearly shows the elemental peaks comprising of majorly Al (94.4%) and Si (5.3%) peaks at the weld position as shown in Fig. 7b, whereas there could be a possibility of intermetallic compounds like Fe_2Si (due to iron impurities in 6XXX series aluminium alloy), Al_2Mn_3 (due to small amount of manganese present in the substrate material) and Mg_2Si (owing to a larger amount of magnesium and silicon present in both substrate and filler wire) as shown in Fig. 7a.

2.3 Metallography

Cross-sectional samples of the welded plate were taken out for metallographic analysis in the perpendicular direction of the weld bead. Different weld zones, i.e. parent metal/base metal (BM), fusion zone (FZ), weld metal (WM) and heat-affected zone (HAZ), were identified and welding flaws such as lack of fusion, porosity, under-cuts were visually checked. Fusion and weld metal could be distinguished by their grain structures and through visuals after a high grade of polishing as shown in Fig. 8. The standard metallographic practice was used to prepare specimens which were etched with Keller's reagent, which consisted of 2.5 ml of HNO_3, 1.5 ml of HCl and 1 ml HF in 95 ml of water for 20 s.

Microstructures were taken from different weld zones such as BM, FZ of 6061-T6 and 6082-T6 aluminium alloy side and WM under distinctive welding process parameters were analysed on an Olympus GX41 metallurgical microscope. In addition to this, FEI Quanta 200F Field Emission Scanning Electron Microscope (FESEM) was performed which was equipped with an energy-dispersive X-ray (EDX) spectrometer engaged to examine the intermetallic bonds/compounds (IMC) which disrupted the mechanical

properties. FESEM examined the morphology and microstructural characterization.

3 Results and Discussions

3.1 Microstructure at Different Weld Zones

The microstructure of parent metal is presented in Fig. 2a–d and e–f which clearly shows the grain boundaries of both the parent materials. Macro-images of welded sample 3, 4 and 5 are shown in Fig. 8, which corresponds to five different positions: A = BM of AA6082-T6, B = FL of AA6082-T6 side, C = weldment (WM), D = FL of AA6061-T6 side and E = BM of AA6061-T6 where microstructure is seen by optical microscope (Table 4) and FESEM (Fig. 9). There is a heterogeneous segregation structure formed in the WM, due to different composition of filler wire as compared to the BM and due to faster cooling rates which are assisted by low heat input in the welded sheets. The WM and FL of 6061-T6 are composed of dendrites with a solid solution of aluminium (α-Al) and an Al–Si eutectic structure as depicted in Fig. 9b and f [36]. Al–Si eutectic structure is a low melting point segregation phase with a lamellar, aggregate, or distinct morphology along the α-Al grain boundary [37]. Al–Si eutectic structure is surrounded by a dendritic structure of α-Al in the WM and FL of 6061-T6 aluminium alloy. Al–Mg phase is existing in the WM as depicted in Fig. 9e. As shown in Fig. 7a, intermetallic compounds formed are Al–Mn (Al_2Mn_3), Fe–Si (Fe_2Si) and Mg–Si (Mg_2Si). Mg_2Si precipitate is formed in the FZ and not in the WM as depicted in Fig. 9d, due to the presence of a high amount of Mg and Si (primary elements) in both the substrate and filler material (ER4043 wire). During fusion welding, in the weld pool, vaporization of alloys takes place, which could cause the loss of alloy elements. Mg being highly evaporative element within such extreme temperature limits (during fusion welding) usually escapes partially from the weld pool. The rest of the Mg reacts with a large amount of Si to form Mg_2Si precipitate as shown in Fig. 7b. Spectrum 10 provides the EDS result for the welded sample 3 (72A, 5.5 mm/s) where the Mg content is considerably reduced to 0.3% (wt%). So, as compared to BM, Mg_2Si precipitate is lower in WM when 6XXX aluminium alloy series is welded with ER4043 filler wire. Iron is also added as an impurity in most of the commercial 6XXX series alloys. As a result, Al–Fe, Al–Mg, Al–Mg–Mn [23, 38, 39], $Al_{0.7}Fe_3Si_{0.3}$, FeNi, $AlFe_{0.23}Ni_{0.77}$ and Fe_2Si possible intermetallic phases could be formed which deteriorates the mechanical properties.

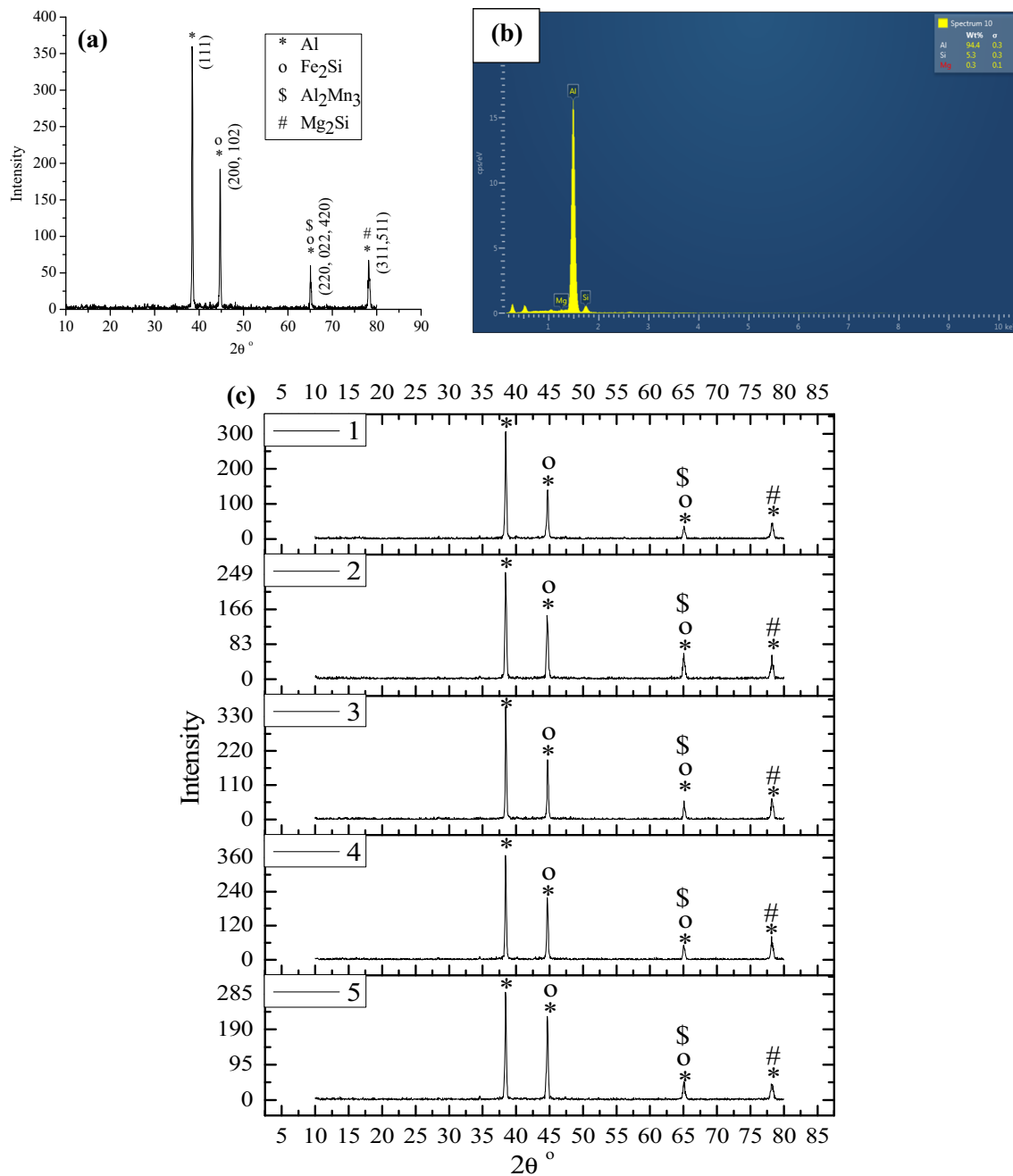**Fig. 7** **a** and **b** XRD plot and EDX spectroscopy of sample 3 (72A, 5.5 mm/s), **c** XRD plot of all samples

3.2 Microhardness (HV)

FISCHERSCOPE HM2000 S is used for microhardness analysis having a diamond indenter. The indenter penetrates the specimen using a load of 300.000mN/20 s with the dwell time of 5 s. Microhardness of the dissimilar welded samples is measured along the line, which is depicted in Fig. 10. Seven points are considered along the hardness measurement line, i.e. BM, HAZ, FL of 6061-T6 side, WM, FL, HAZ, BM of 6082-T6 side. At least five indentations of each sample are taken and then the average values are utilized to calculate microhardness at a specific zone of that sample. Almost all the samples are having approximately similar microhardness in their respective zones. The microhardness values of WM in both sides are approximately 50HV at the centre and 70HV within the weld terminals which is higher as compared to MIG welding (52HV) obtained by Ishak et al. [40]. At FL, it is similar on both sides (approximately 70HV) and at HAZ (approximately 80-85HV at 6082-T6 side and 70-75HV at
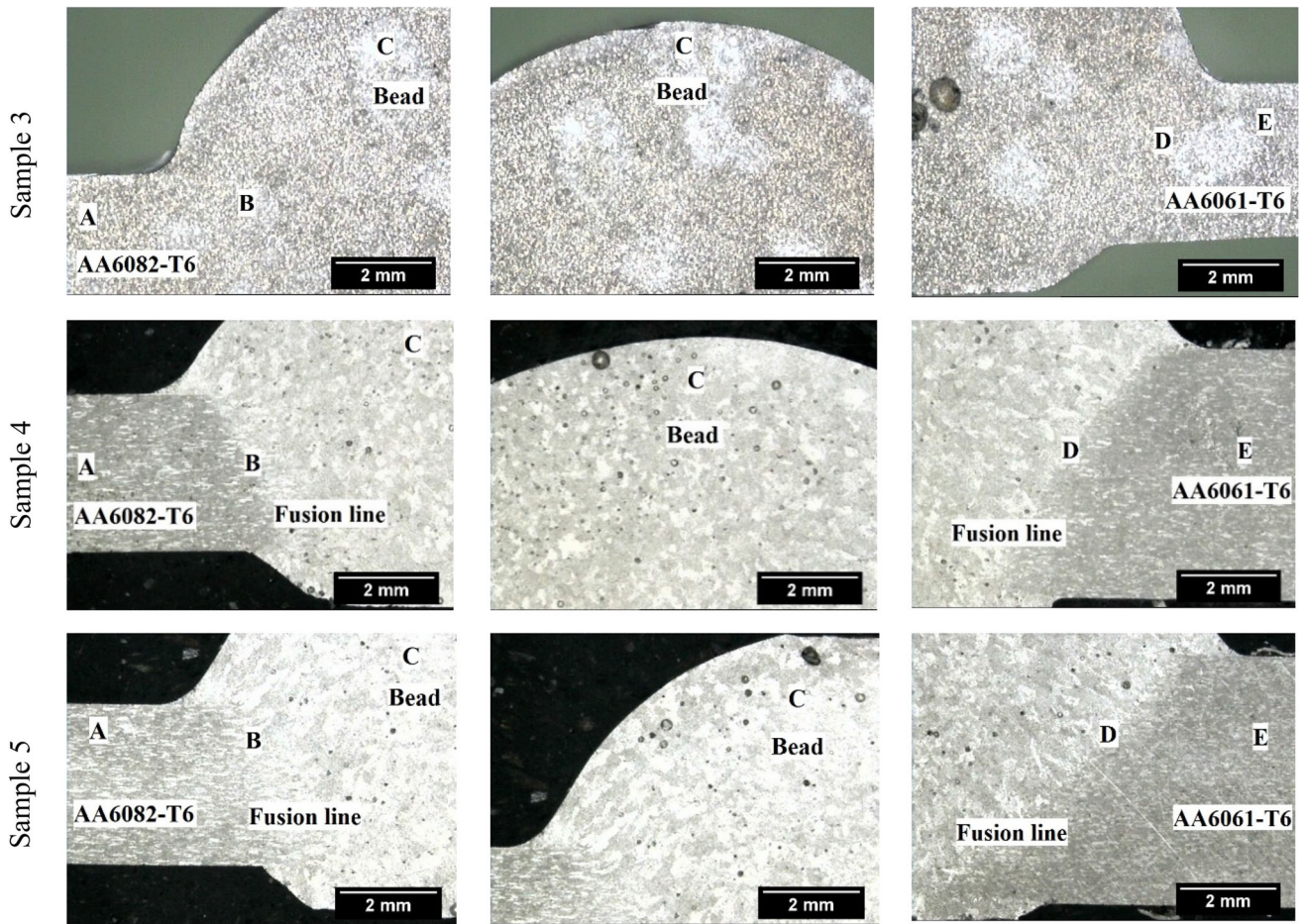
Fig. 8 Macro-images of welded samples 3, 4 and 5 indicating the points

Table 4 Microstructure of different positions by Optical microscope

	A	B	C	D	E
3WR					
4WR					
5WR					

A= AA6082-T6 BM; B= AA6082-T6 side Fusion Line (FL); C= weldment (WM); D= AA6061-T6 side Fusion Line (FL); E= AA6061-T6 BM; WR=With reinforcement.

Fig. 9 FESEM images of sample 3WR **a** and **b** FL of AA6061-T6 side; **c** and **d** FL of AA6082-T6 side; **e** and **f** weldment (WM)
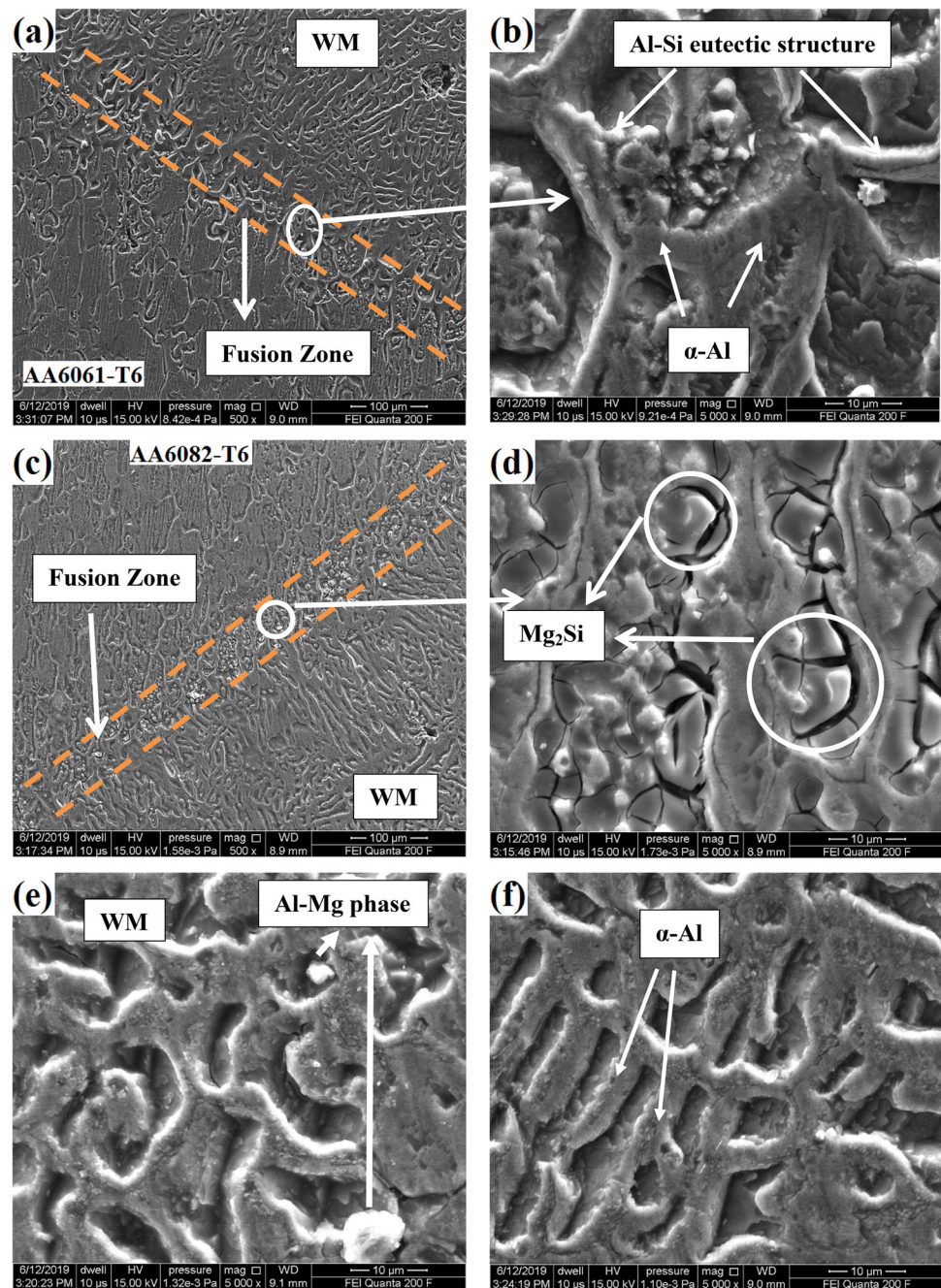
6061-T6 side) compared to BM (80-85HV at 6082-T6 and 65-70HV at 6061-T6). Before welding the microhardness of parent metal AA6082-T6 is 109 ± 9HV and AA6061-T6 is 116 ± 9HV. It undergoes softening behaviour which ultimately reduces its hardness value during and post welding. The deviation in microhardness majorly depends on the different zone on the welded sample due to possible reasons like softening of HAZ, course or large grain structure, precipitate formation, brittle intermetallic compound formation, etc. During the solidification of FZ, the metal usually eludes its original strength due to strain-hardening effect (SHE). Development of intermetallic compounds (IMC) like Mg_2Si, which is brittle in nature, in the FZ, excites a growth in microhardness specifically in aluminium alloys. The possibility of precipitate formation of Mg_2Si is more in FZ and HAZ as contrasted to BM as depicted in Fig. 9d, which results in a slight decrease in microhardness. Softening behaviour in HAZ and FL of aluminium alloys also changes the microstructure due to which it is called as the weakest zone of the joint [37]. In
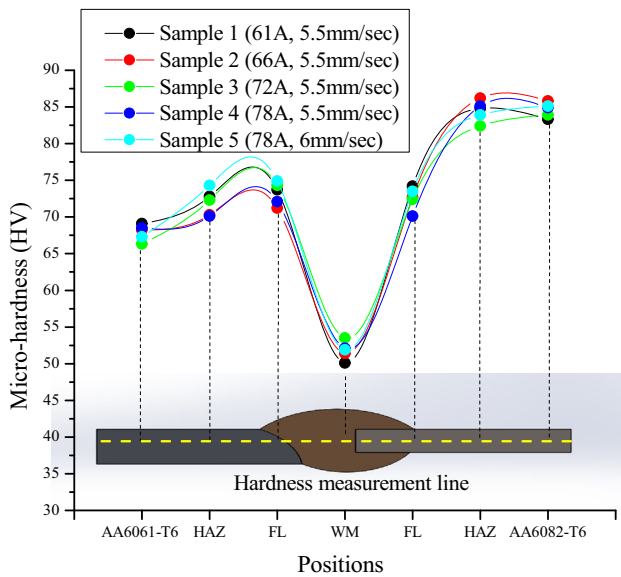
Fig. 10 Microhardness profile with respect to weld positions

FZ of 6082-T6 aluminium alloy side, there is the existence of Mg_2Si after welding, whereas in FZ of 6061-T6 aluminium alloy side, the Mg_2Si phases dissolute which results in the development of large precipitate and coarsening of grains [24, 41]. Therefore, the microhardness of FZ and HAZ of 6082-T6 side is higher than FZ and HAZ of 6061-T6 aluminium alloy. The cumulative effect is considered for microhardness, i.e. as compared to BM of 6082-T6, HAZ and FZ are having lower microhardness, whereas 6061-T6 side experiences the negligible difference. It can be inferred from the above discussion that 6061-T6 is more heat sensitive than 6082-T6 aluminium alloy [37]. From Fig. 10, due to grain size refinement (coarser grains), the microhardness of WM is lower (approximately 30%) as compared to HAZ. Due to rapid cooling rate, the grains become finer (as moved from WM to BM of both the substrate material) for enhancement of the microhardness values in the HAZ and FL. The rise in microhardness values at HAZ and FL is due to rapid

cooling rate (as heat input decreases while going from WM to BM), leading to the development of reduced grain size. As there is the minimum change in the microhardness with respect to the heat input values taken in this paper, Fig. 10 shows the microhardness at different position of the specimen.

3.3 Mechanical Evaluation of Joints

Tensile specimens are taken as per ASTM E8 standards as shown in Fig. 11. The 50KN capacity of TINIUS OLSEN UTM H50KS was used to measure the tensile strength of the joint with a ram speed of 1 mm/min. Tensile specimens, taken in a transverse direction with and without reinforcement, were tested in order to find the joint integrity. Figure 12a and b shows a tensile specimen of samples with reinforcement, and Fig. 12c and d shows a tensile specimen of welded samples without reinforcement. Tensile strength of sample 3 is the highest with respect to the rest of the samples having heat input of 120.43 J/mm. Tensile specimen taken in a transverse and longitudinal direction for sample 3 results in a 10% increase in the longitudinal direction without reinforcement. Tensile specimen is with reinforcement (184 MPa) and without reinforcement (201.67 MPa) in transverse direction for sample 3. Ishak et al. [40] experimentally investigated the maximum tensile strength of 200.66 MPa while using ER4043 wire in MIG welding of 6061 aluminium alloy. Almost 12% and 8% increase in sample 4 and 5, respectively, in transverse direction without reinforcement, signifies the joint integrity. Figure 13 displays the stress vs strain curve for welded samples with and without reinforcement. For without reinforcement (WOR) specimens, samples 1, 2 and 4 broke from the bead, whereas samples 3 and 5 broke from AA6082-T6 side. It can be noticed that the percentage elongation of sample 3 and 5 is maximum with respect to other samples in both with and without reinforcement that increases ductility. Samples, which broke from AA6082-T6 side, show the bead strength and

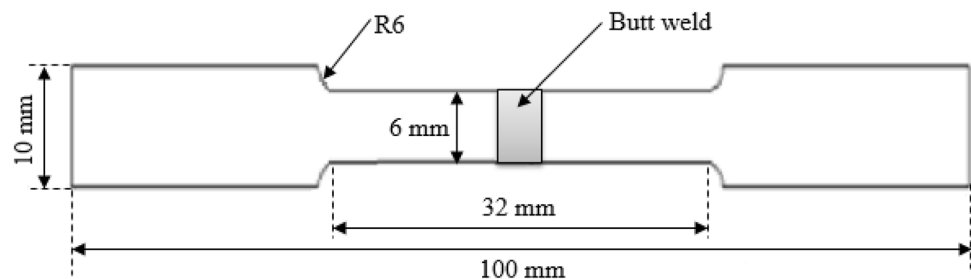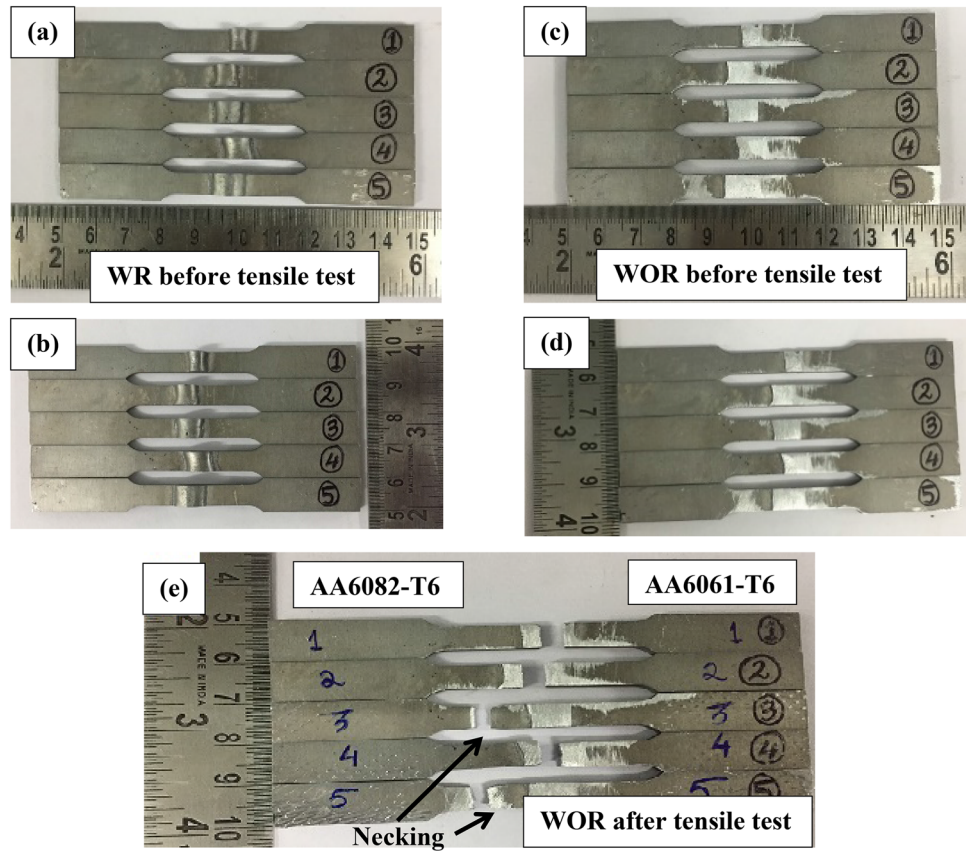**Fig. 11** Tensile specimen as per ASTM E8

Fig. 12 Tensile specimen **a** and **b** with reinforcement (WR), **c** and **d** without reinforcement (WOR), **e** after tensile test WOR specimen

joint efficiency. Compared to MIG welding, CMT is achieving higher tensile strength with lower heat input. Mg_2Si is the brittle intermetallic compound responsible for the joint fracture.

Table 5 shows the tensile strength of CMT welded samples with and without reinforcement with their respective percentage elongations. Higher efficiency of the joint results in the finest weld quality. Samples 3, 4 and 5 give the joint efficiency of above 60%, which is acceptable for the industrial applications. Sample 3 has the highest joint efficiency (64.78% with reinforcement, 71.01% without reinforcement and 71.30% in the longitudinal direction without reinforcement) among the rest as shown in Fig. 14. The process parameters for sample 3 (72A current and 5.5 m/s welding speed), 4 (78A and 5.5 m/s) and 5 (78A and 6 m/s) are suitable with respect to the rest of the two samples. Welding process parameters of sample 3 are optimal which gives great results. The welded joint is relatively weaker than the parent material due to potential defects occurring at the time of weldings such as porosity, slag inclusions, and others. These defects can be examined by various non-destructive techniques (NDT).

3.4 Residual Stress

PULSTEC micro-X360n Full 2D based on the high-resolution X-ray diffraction technique as shown in Fig. 15, has been used to calculate the residual stresses by $\cos\alpha$ method. Residual stress is the stress that is endured within a material in the dearth of exterior forces or thermal gradients after manufacturing and material processing. It can be measured by this technique, which uses a solitary exposure to accumulate the absolute diffraction cone through a 2D detector. Since there are many non-destructive techniques to determine the residual stress, X-ray diffraction is suitable for thin plates as its penetration is about 10 μm with a range of 10 μm to 1 mm of spatial resolution. Standard chromium (Cr) material X-ray tube has been used having collimator size of 1 mm diameter with 30 kV and 1 mA specification.

As illustrated in Fig. 16, compressive residual stress is maximum at the bead as compared to FZ and BM due to the higher cooling rate. Figure 17a and b exemplifies the image of the sample, Debye–Scherrer ring (3D), 2D distortion graph and residual profile of sample 2 (108.48 J/mm) and 5 (126.88 J/mm) are attained during residual stress test analysis. Debye–Scherrer ring (3D) signifies the
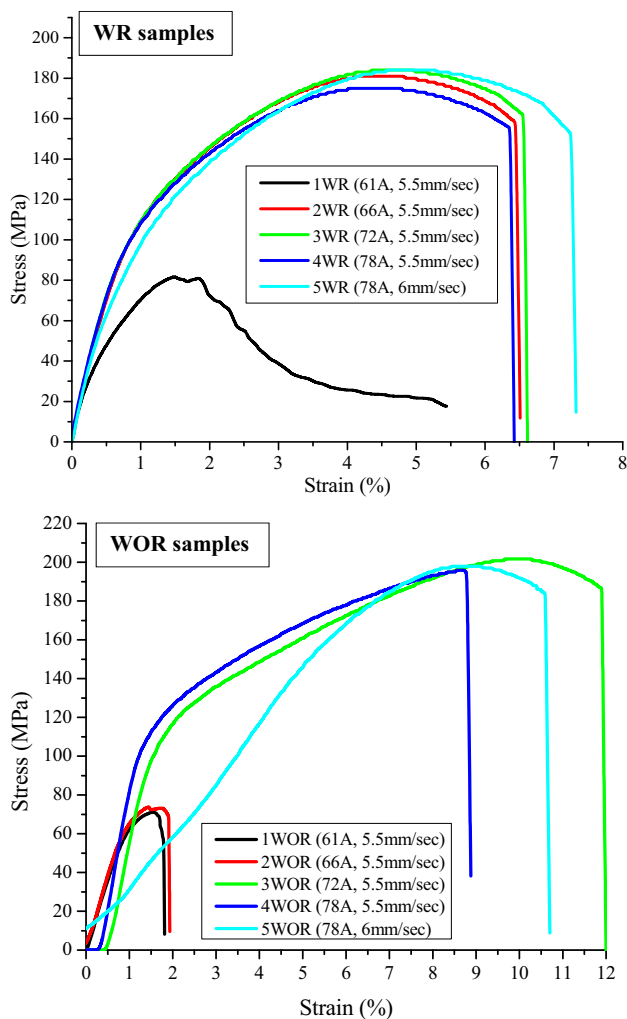
Fig. 13 Stress vs strain curve for welded samples with (WR) and without reinforcement (WOR)

concentration of residual stress at weld bead, which is demonstrated by converting red (at the tip) to blue shade (at the bottom). Red shade indicates that there is more concentration of residual stress in that region, whereas blue shade reveals the negligible concentration of residual stress. The position of the Debye rings, which is a direct measure of strain, can accurately measure residual stress. With the help of Debye ring's spotted position, the extent of the strain is governed. The distortion image acquired in 108.48 J/mm indicates that high amount of destruction, i.e. structural variations has occurred in the sample because of the high amount of compressed residual stresses, indicated by the profile peak in the profile image. 126.88 J/mm of heat input indicates a better distortion image as compared with 108.48 J/mm due to less amount of compressed residual stresses. Koli et al. [42] compared residual stress between CMT, MIG pulse synergic and MIG manual and found that CMT shows lesser residual stress as compared to the other two welding process. The optimized parameter is sample 3 (72A current and 5.5 mm/s welding speed with heat input 120.43 J/mm) because of its highest tensile strength with and without reinforcement (184 MPa and 201.67 MPa). Sample 3 has good microhardness and residual stress at various positions of the weld bead.

4 Conclusions

Dissimilar aluminium alloy joining by CMT is the prime objective of this paper with higher mechanical properties as compared to other welded samples with different process parameters.

Table 5 Tensile strength results of the CMT welded with and without reinforcement

S.No.	V (V)	I (A)	WFS (m/min)	S (mm/s)	H (J/mm)	Tensile Strength (MPa)	% elongation	Fracture Location	Joint efficiency (%) AA6061-T6 (284 MPa)	AA6082-T6 (304 MPa)
1WR	11.2	61	4.2	5.5	99.37	81.7	5.44	Weld	28.76	26.875
1WOR	11.2	61	4.2	5.5	99.37	71	1.79	Weld	25	23.35
2WR	11.3	66	4.7	5.5	108.48	181	6.45	HAZ	63.73	59.53
2WOR	11.3	66	4.7	5.5	108.48	73.75	1.92	Weld	25.96	24.25
3WR	11.5	72	5.1	5.5	120.43	184	6.57	HAZ	64.78	60.52
3WOR	11.5	72	5.1	5.5	120.43	201.67	12	HAZ	71.01	66.33
3L	11.5	72	5.1	5.5	120.43	202.5	34.9	C	71.30	66.61
4WR	12.2	78	5.4	5.5	138.41	175	6.37	HAZ	61.61	57.56
4WOR	12.2	78	5.4	5.5	138.41	195.83	8.80	Weld	68.95	64.41
5WR	12.2	78	5.4	6	126.88	184	7.26	HAZ	64.78	60.52
5WOR	12.2	78	5.4	6	126.88	198	10.7	HAZ	69.54	64.96

Arc length correction (ALC) factor is taken as zero for all samples; contact tip to workpiece distance (CTWD) is 10 mm for all samples; shielding gas is kept constant (15 l/min) for all samples; WR = with reinforcement; WOR = without reinforcement; L = longitudinal without reinforcement; HAZ = heat-affected zone; C = centre of the weld in the longitudinal direction
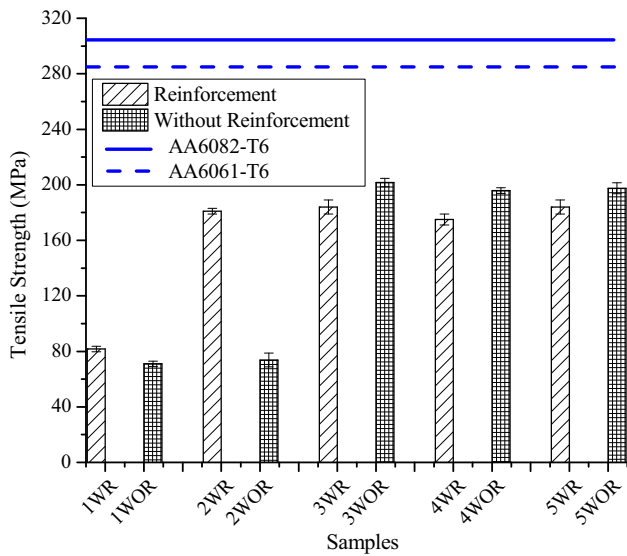
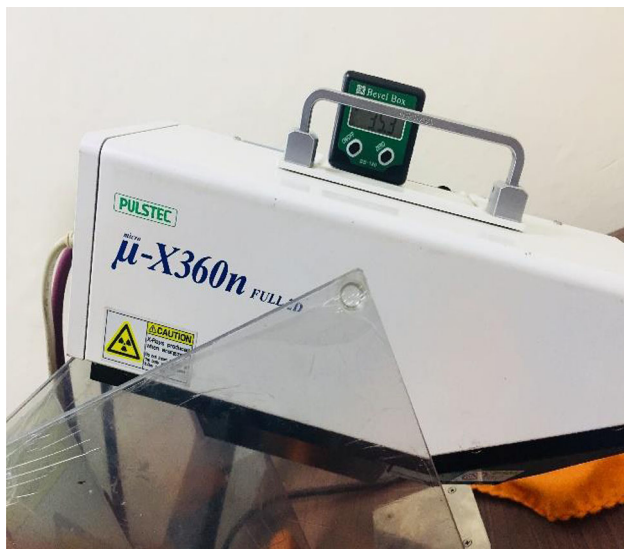Fig. 14 Tensile strength of CMT welded sample with (WR) and without reinforcement (WOR)

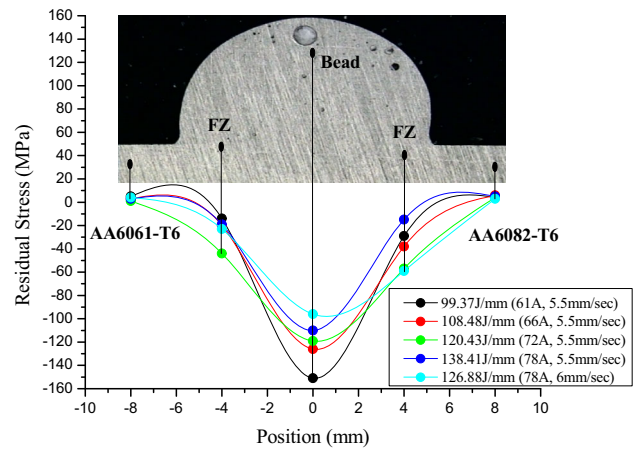Fig. 15 High-resolution X-ray diffraction machine

Fig. 16 Residual stress on the position of the weld bead

m/min; welding/travel speed = 5.5 mm/s; heat input = 120.43 J/mm.

3. Tensile strengths of samples 3 (72A current and 5.5 m/s welding speed), 4 (78A and 5.5 m/s) and 5 (78A and 6 m/s) are higher as compared to samples 1 and 2 for both with and without reinforcement due to sufficient heat input that leads to better penetration. Sample 3 (120.43 J/mm) has the highest joint efficiency (64.78% with reinforcement, 71.01% without reinforcement and 71.30% in the longitudinal direction without reinforcement) among the rest. Removing the reinforcement helps in increasing the tensile strength to about 7–11%.

4. FESEM and optical microscope images of microstructure validate that the high amount of silicon and magnesium contents is present at weldment and fusion line of both the substrate side, which tends to form a brittle intermetallic compound (Mg_2Si). As a result, the joint fracture can take place.

5. In the case of welded samples, increased hardness is observed in the fused zone due to the development of brittle intermetallic compound (IMC). The weld metal shows lower hardness in comparison with the heat-affected zone due to its grain size being more refined. The faster cooling rate results in finer grain size, which results in higher hardness value in the heat-affected zone and fusion line.

6. Residual stress shows higher compressive values at the bead as compared to the fusion zone and base metal in all the welded samples.

1. Dissimilar aluminium alloys with dissimilar thickness has been joined successfully using cold metal transfer with the help of aluminium–silicon wire.

2. The optimal welding parameter for relatively high mechanical properties is sample 3 having voltage = 11.5 V; current = 72A; wire feed speed = 5.1

(a) 108.48J/mm · **Debye Scherrer Ring (3D)** · **Distortion graph** · **Residual profile**

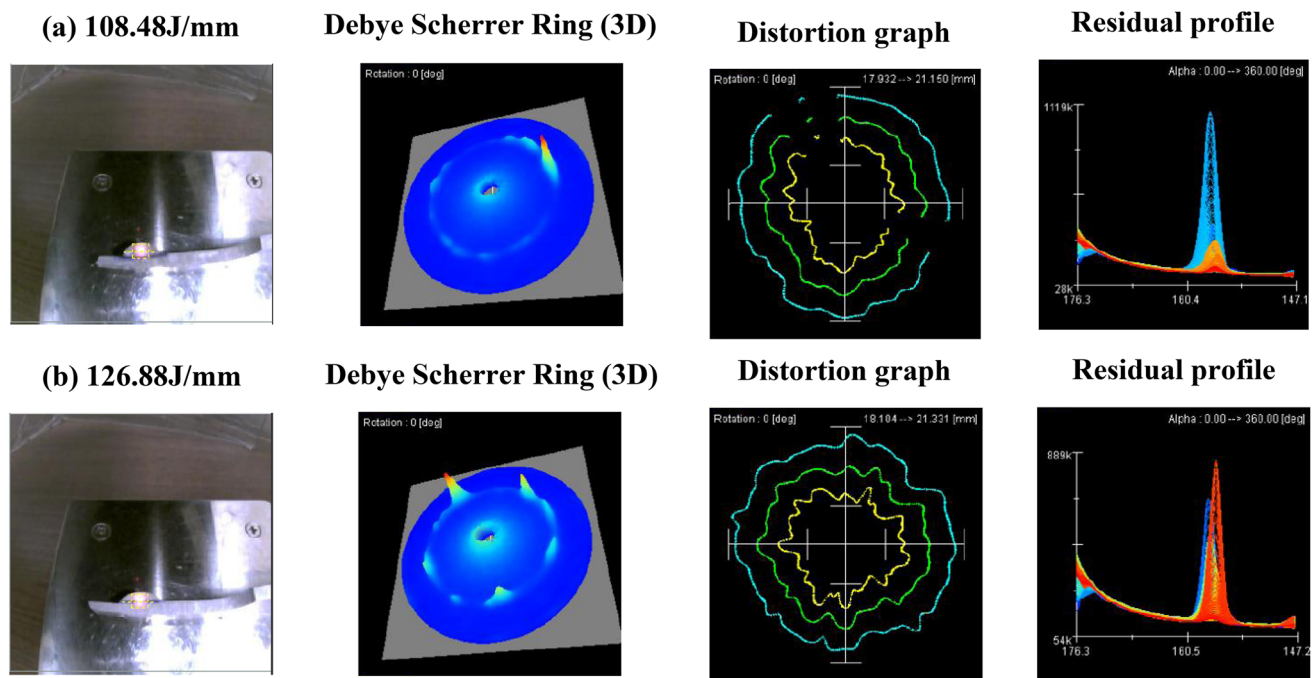**(b) 126.88J/mm** · **Debye Scherrer Ring (3D)** · **Distortion graph** · **Residual profile**

Fig. 17 **a** and **b** sample image, Debye–Scherrer ring, distortion graph and residual profile of sample 2 (108.48 J/mm) and 5 (126.88 J/mm) at weld bead

References

1. İrizalp A O, Durmuş H, Yüksel N, and Türkmen İ. *Matéria (Rio de Janeiro)* **21** (2016) 615.
2. Schierl A. *Weld. World Lond.* **49** (2005) 38.
3. Feng J, Zhang H, and He P. *Mater Des.* **30** (2009) 1850.
4. Fang J, Gao Y, Sun G, and Li Q. *Finite Elements Anal. Des.* **67** (2013) 13.
5. Totten G E, and MacKenzie D S. *Handbook of Aluminum: Physical Metallurgy and Processes*. CRC press, New York (2003).
6. Kaufman J G. *Introduction to Aluminum Alloys and Tempers*. ASM international, Cleveland (2000).
7. Mathers G. *The welding of Aluminium and Its Alloys*. Woodhead Publishing, Sawston (2002).
8. Mossman M M, and Lippold J C. Weld. J. New York **81** (2002) 188.
9. Pickin C G, Williams S W, Lunt M. *J Mater Process Technol* **211** (2011) 496.
10. Hermans M J M, and Den Ouden G. Weld. J New York (1999)137.
11. Li-Li G, Ling-Shen F, and Ming-Yang, Z. . Research on the line of laser tailor welded blanks. In Information Engineering and Applications: (2012) 315–322.
12. Gery D, Long H, and Maropoulos P. *J Mater Process Technol* **167** (2005) 393.
13. Aslanlar S, Ogur A, Ozsarac U, Ilhan E, and Demir Z. *Mater Des* **28** (2007) 2.
14. Xia M, Tian Z, Zhao L, and Zhou Y N, *Mater Trans* **49** (2008) 746.
15. Liu J, Wang A, Zheng Y, Liu X, Gandra J, Beamish K, Petre A, and Wang L L *Procedia Eng* **207** (2017) 729.
16. Moulton J A, and Weckman D C, Weld J **89** (2010) 11.
17. Sterjovski Z, Bayley C, Donato J, Lane N, and Lang D. Weld-end solidification cracking in pulsed-tandem gas metal arc welding of naval steels (2014).
18. Liu X, Frankel G S, Zoofan B, and Rokhlin S I. *Corros Sci* **49** (2007) 139.
19. Shu F, Lv Y, Liu Y, Xu F, Sun Z, He P, and Xu B, *Construct Build Mater* **54** (2014) 224.
20. Petroyiannis P V, Kamoutsi E, Kermanidis A T, Pantelakis S G, Bontozoglou V, and Haidemenopoulos G N. *Fatigue Fracture Eng Mater Struct* **28** (2005) 565.
21. Lynch S P. *Acta Metall* **36** (1988) 2639.
22. Moreira P M G P, Santos T, Tavares S M O, Richter-Trummer V, Vilaça P, and De Castro P M S T, *Mater Des* **30** (2009) 180.
23. Elrefaey A, and Ross N G. *Acta Metallurgica Sinica (English Letters)* **28** (2015) 715.
24. Ahmad R, and Bakar M A. Mater Des **32** (2011) 5120.
25. Cook G E, and Eassa H E D E *IEEE Trans Ind Appl* (5) (1985) 1294.
26. Mendez P F, and Eagar T W. *Adv Mater Process* **159** (2001) 39.
27. Quintino L, Liskevich O, Vilarinho L, and Scotti A. *Int J Adv Manufact Technol* **68** (2013) 2833.
28. Joseph A, Harwig D, Farson D F, and Richardson R. *Sci Technol Weld J* **8** (2003) 400.
29. Cao R, Yu G, Chen J H, and Wang P C, *J Mater Process Technol* **213** (2013) 1753.
30. Cao R, Feng Z, Lin Q, and Chen J H, *Mater Des* **56** (2014) 165.
31. Wang J, Feng J C, and Wang Y X. *Mater Sci Technol* **24** (2008) 827.
32. Lorenzin G, and Rutili G. *Weld Int* **23** (2009) 622.
33. Lin J, Ma N, Lei Y, and Murakawa H. *J Mater Process Technol* **213** (2013) 1303.
34. Yang S, Zhang J, Lian J, and Lei Y. *Mater Des* **49** (2013) 602.
35. Gungor B, Kaluc E, Taban E, and Aydin S I K. *Mater Des* **54** (2014) 207.

36. Liang Y, Shen J, Hu S, Wang H, and Pang J. *J Mater Process Technol* **255** (2018) 161.
37. Nie F, Dong H, Chen S, Li P, Wang L, Zhao Z, Li X, and Zhang H. *J Mater Sci Technol* **34** (2018) 551.
38. Eskin D G. *Physical Metallurgy of Direct Chill Casting of Aluminum Alloys*. CRC Press, Boca Raton (2008).
39. Mondolfo L F. Aluminium alloys: structure and properties. Butter Worths, London, 1. Ausgabe S: 72 (1976).
40. Ishak M, Noordin N F M, Razali A S K, Hakim L, and Shah A. The effect of filler ER4043 and ER5356 on weld metal structure of 6061 aluminium alloy by Metal Inert Gas (MIG). methanol yield over Bi2S3/CdS photocatalyst:4 (2015).
41. Maisonnette D, Suery M, Nelias D, Chaudet P, and Epicier T. *Mater Sci Eng A* **528** (2011) 2718.
42. Koli Y, Yuvaraj N, Aravindan S. *Mater Res Express* **6** (2020) 1265e5.